# Anisotropic Dirac Fermions in a Bi Square Net of $SrMnBi_2$

Joonbum Park,[1] G. Lee,[2] F. Wolff-Fabris,[3] Y. Y. Koh,[4] M. J. Eom,[1] Y. K. Kim,[4] M. A. Farhan,[2] Y. J. Jo,[5] C. Kim,[4] J. H. Shim,[2,*] and J. S. Kim[1,†]

[1]*Department of Physics, Pohang University of Science and Technology, Pohang 790-784, Korea*
[2]*Department of Chemistry, Pohang University of Science and Technology, Pohang 790-784, Korea*
[3]*Dresden High Magnetic Field Laboratory, Helmholtz-Zentrum Dresden-Rossendorf, D-01314 Dresden, Germany*
[4]*Institute of Physics and Applied Physics, Yonsei University, Seoul 120-749, Korea*
[5]*Department of Physics, Kyungpook National University, Daegu 702-701, Korea*

(Received 27 April 2011; published 16 September 2011)

We report the observation of highly anisotropic Dirac fermions in a Bi square net of $SrMnBi_2$, based on a first-principles calculation, angle-resolved photoemission spectroscopy, and quantum oscillations for high-quality single crystals. We found that the Dirac dispersion is generally induced in the $(SrBi)^+$ layer containing a double-sized Bi square net. In contrast to the commonly observed isotropic Dirac cone, the Dirac cone in $SrMnBi_2$ is highly anisotropic with a large momentum-dependent disparity of Fermi velocities of $\sim 8$. These findings demonstrate that a Bi square net, a common building block of various layered pnictides, provides a new platform that hosts highly anisotropic Dirac fermions.

DOI: 10.1103/PhysRevLett.107.126402 PACS numbers: 71.20.Ps, 71.18.+y, 72.20.My

Unlike commonly observed quadratic dispersions, a *linear* energy dispersion, similar to the spectrum of relativistic Dirac particles, is found in the so-called Dirac materials such as graphene and topological insulators. Linearly extended bands in Dirac cones, along with the (pseudo)spins, determine the peculiar properties of Dirac materials. For example, backscattering is strongly suppressed, leading to a high electron mobility, and anomalous half-integer quantum Hall effects are observed with a nonzero Berry's phase [1,2].

While the Dirac cones in graphene and topological insulators are in general isotropic ones, different types of Dirac cones have been proposed recently. A highly anisotropic Dirac cone was theoretically predicted in graphene under external periodic potentials [3] or mechanical stress [4]. Tilted Dirac cones have been suggested in a layered organic conductor $\alpha$-$(BEDT\text{-}TTF)_2I_3$ at high pressures [5]. As a hybrid case, a semi-Dirac cone with a quadratic dispersion in one direction and linear in the other may appear in hypothetical graphene with a particular set of hopping parameters between the nearest neighbors [6]. The presence of such a hybrid Dirac cone has been proposed in quantum confined $VO_2/TiO_2$ nanostructures [7]. While the realization of these Dirac fermions may lead to a discovery of novel electronic states, e.g., a new type of quantum Hall state [8], there has not been a direct experimental observation of the above-mentioned Dirac fermions.

In this Letter, we report on a new bulk Dirac material $SrMnBi_2$ that hosts highly anisotropic Dirac fermions in its Bi square net. Based on results from a first-principles calculation, quantum oscillations, and angle-resolved photoelectron spectroscopy (ARPES) on high-quality single crystals, we demonstrate that there is a Dirac dispersion in the electronic structure of the double-sized Bi square net. The Dirac electrons have pseudospins stemming from wave-function amplitudes at two different sublattices, similar to the case of graphene. In contrast to the graphene case, however, the Dirac cone in $SrMnBi_2$ is highly anisotropic, showing a significant momentum-dependent Fermi velocity ($v_F$) with a ratio between the maximum and minimum $v_F$'s of $\sim 8$. These findings suggest that the Bi square net, a common building block of various layered compounds [9], can provide a new platform for highly anisotropic Dirac fermions.

Single crystals of $SrMnBi_2$ were grown by slow cooling of melted stoichiometric mixtures of Sr (99.99%), Mn (99.9%), and Bi (99.999%) chunks in a sealed quartz ampoule. X-ray diffraction and energy dispersive spectroscopy confirm high crystallinity [10] [Fig. 1(d)] and right stoichiometry. Magnetotransport properties were measured in a 6-probe configuration under magnetic fields up to static 33 T at National High Magnetic Field Laboratory and up to pulsed 63 T at Dresden High Magnetic Field Laboratory. ARPES data were taken with 24 eV photons at beam line 5-4 of Stanford Synchrotron Radiation Laboratory. Samples were cleaved *in situ* in an ultrahigh vacuum ($<4 \times 10^{-14}$ Torr). First-principles calculations were done by using the full-potential linearized augmented plane wave method [11] in the WIEN2K package [12]. The generalized gradient approximation was utilized for the exchange correlation potential [13].

We first look at the basic electronic properties of $SrMnBi_2$. $SrMnBi_2$ consists of a MnBi layer with edge-sharing $MnBi_4$ tetrahedrons and a two-dimensional (2D) Bi square net stacked with Sr atoms as shown in Fig. 1(a). Because of the low electronegativity of Sr, ionic Sr layers electronically separate the MnBi layers and the Bi square net. In the $[MnBi]^-$ layer, $Mn^{2+}$ has a half filled $3d^5$

 

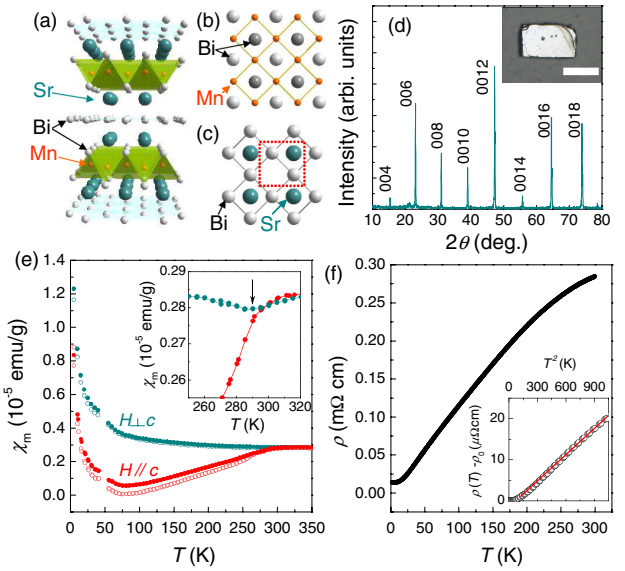


FIG. 1 (color online). (a) $SrMnBi_2$ crystal structure with two building blocks of (b) a MnBi layer and (c) a Bi square net. Note the double-sized unit cell in the Bi square net. (d) X-ray diffraction pattern from basal planes of a cleaved crystal, showing only (00$l$) reflections. An optical image of a crystal with a scale of 250 $\mu$m is shown in the inset. (e) Magnetic susceptibilities $\chi(T)$ at $H = 1$ T parallel and perpendicular to the $c$ axis in zero-field-cooled (open) and field-cooled (solid) runs. A kink in $\chi(T)$ at $T_N \sim 290$ K is clearly seen in the inset. (f) In-plane resistivity $\rho(T)$. It follows a quadratic $T$ dependence at low temperatures as shown in the inset.

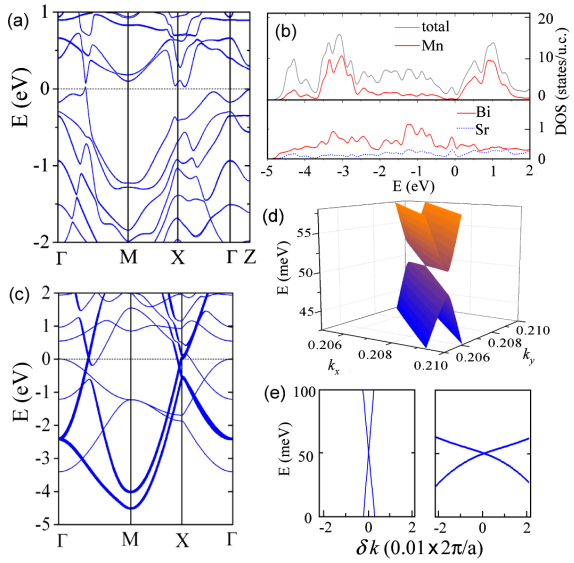


FIG. 2 (color online). (a) Band structures of $SrMnBi_2$ and (b) total (gray line) and local Mn (red solid line) DOS are shown in the upper panel. The lower panel shows local DOSs at Bi (red solid line) and Sr (blue dashed line) sites in the SrBi layer. (c) Band structure of the isolated $(SrBi)^+$ layer where the line thickness represents the Bi $6p_{x,y}$ orbital character. (d) Anisotropic energy surfaces around the Dirac point $k_0 = (0.208, 0.208)$ for the $(SrBi)^+$ layer. (e) Dispersions near the Dirac point parallel or perpendicular to the $\Gamma$-$M$ symmetry line. SOC in the Bi bands is turned on for the results in (a) and (b), while SOC is not considered for the results in (c), (d), and (e).

configuration. The strong Hund coupling of $Mn^{2+}$ leads to a magnetic ground state in Mn$P$ ($P$ denotes pnicotgen) layers [14]. Magnetic susceptibility $\chi(T)$ in fact exhibits a kink at $T_N \sim 290$ K [Fig. 1(e)], indicating an antiferromagnetic transition. With the antiferromagnetic ordering, the charge conduction in MnBi layers is highly suppressed. On the other hand, the covalent nature of Bi $6p$ bonds in the 2D square net makes the plane conducting, thus governing the transport properties. Resistivity $\rho(T)$ in Fig. 1(f) indeed shows a highly metallic behavior, that is, a quadratic temperature dependence of $\rho(T) = \rho_0 + AT^2$. The parameter $A$, which is inversely proportional to the Fermi temperature, is 19(1) n$\Omega$ cm K$^{-2}$, comparable to that of pure Bi [15]. This suggests that light carriers are responsible for the metallic conduction.

The electronic structure of $SrMnBi_2$ from a first-principles calculation clearly reveals the origin of the light carriers. From the comparison of the total energies for several magnetic states, we find that a Néel-ordered state in the MnBi layer is the most stable state [16]. With a Néel ordering in the MnBi layer, we calculate the band structures of $SrMnBi_2$ with the spin-orbit coupling (SOC) taken into account for the Bi bands [Fig. 2(a)]. Because of the large spin polarization of Mn $3d$ electrons, Mn bands are placed away from the Fermi level ($E_F$) as seen in the density of states (DOS) in Fig. 2(b). The states near $E_F$ are dominated by the Bi states in the square net where the Dirac-like energy dispersion is clearly seen at $k_0 = (0.208, 0.208)$. A small gap near the Dirac point appears only when the SOC is taken into account, suggesting that this gap is not due to the orbital hybridization but from the SOC. Therefore, the light carriers are Dirac fermions residing in the 2D Bi square net.

In order to investigate the nature of the Dirac fermions in the Bi square net, we calculate the band structure of a single $(SrBi)^+$ layer composed of a Bi square net stacked with Sr atoms above and below and plot it in Fig. 2(c). For the sake of clarity, we did not include the SOC in this case. We note that Dirac cones exist at several $k$ points, but only one at $k_0 = (0.208, 0.208)$ retains the Dirac dispersion in the band structure of $SrMnBi_2$. Therefore, we focus on the Dirac cone at $k_0$. Near the $E_F$, states have mainly Bi $6p_{x,y}$ character with a small contribution from Sr $4d$ orbitals due to hybridization. There are two *identical* Bi atoms per unit cell because Sr atoms below and above the square net cause unit cell doubling. This leads to folding of the dispersive Bi $6p$ bands and makes the two Bi $6p_{x,y}$ bands cross each other. The Sr-Bi hybridization lifts the degeneracy of the folded bands except the momentum space along the $\Gamma$-$M$ symmetry line, resulting in the formation of the Dirac cone.

There, the pseudospin of the Dirac cone can be defined as the amplitude of the wave function at different Bi sublattices, similar to the graphene case.

In spite of the similarity to graphene, there are differences. First of all, the Dirac cone $SrMnBi_2$ is highly anisotropic as seen in the Dirac dispersion of the $(SrBi)^+$ layer in Fig. 2(d). Along the $\Gamma$-$M$ symmetry line, the Fermi velocity is $v_F^{\parallel} = 1.51 \times 10^6$ m/s, which is comparable to that of graphene. In contrast, the dispersion along the cut perpendicular to the $\Gamma$-$M$ line is much weaker with $v_F^{\perp}$ of $\sim 1.91 \times 10^5$ m/s, a factor of $\sim 8$ reduction compared to $v_F^{\parallel}$. The anisotropic nature of the Dirac cone is firmly retained in the full band structure of $SrMnBi_2$. The existence of such anisotropy stems from the fact that the dispersion along the $\Gamma$-$M$ line is determined by overlap between the neighboring Bi atoms in a square net while that normal to the $\Gamma$-$M$ line is due to the hybridization between Sr $d_{xz,yz}$ orbitals and Bi $p_{x,y}$ orbitals. Therefore, the Dirac dispersion in a double-sized Bi square net is always highly anisotropic [17]. Another difference is the SOC gap. Unlike the negligible SOC gap in graphene [18], there is a sizable SOC gap of $\sim 40$ meV at the Dirac point in $SrMnBi_2$. This implies that $SrMnBi_2$ is a system with a SOC-induced gap at the Dirac point, where a large spin Hall effect can be produced [19]. These differences clearly demonstrate that the Dirac cone in the Bi square net of $SrMnBi_2$ is distinct from that in graphene.

In order to experimentally investigate the electronic structure, we performed ARPES experiments on $SrMnBi_2$ crystals. Figure 3(a) shows a Fermi surface (FS) map obtained by integrating the ARPES intensity within a 25 meV energy window about the $E_F$. There are two distinct regions with high photoemission intensities: large circular FS centered at the $\Gamma$ point and a needlelike one between the $\Gamma$ and $M$ points. To compare the data with the calculation, we plot calculated FSs in Fig. 3(b). There are three small FSs: needle-shaped FSs on the $\Gamma$-$M$ line and near the $X$ point and flower-shaped hole pockets near the $Z$ point. In comparison with the calculated FSs, the large FS near the $\Gamma$ point should come from the flower-shaped pockets near the $Z$ point, as the momentum resolution along the $k_z$ direction is relatively poor due to the finite escape depth of the photoelectrons. The needlelike FS on the $\Gamma$-$M$ line, on which we focus, is consistent with the calculated FS. On the other hand, the calculated FSs near the $X$ point, which originated from a band bottom, are not observed. The discrepancy is most likely due to the underestimation of the band gap near the $X$ point in the generalized gradient approximation exchange correlation functional.

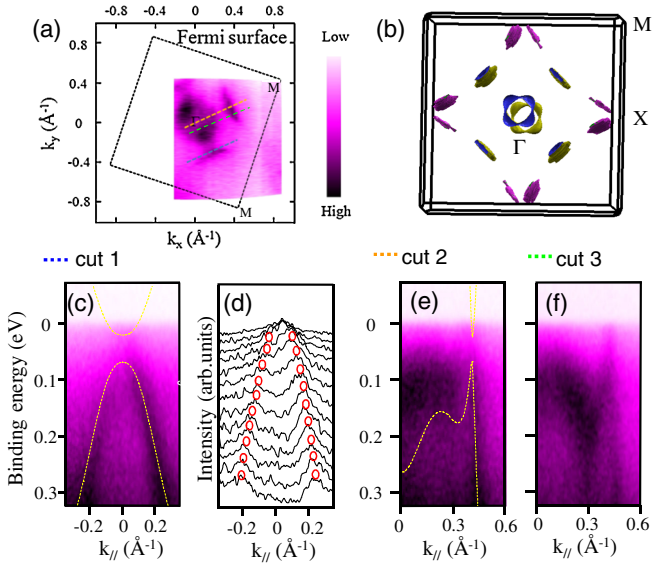


FIG. 3 (color online). (a) ARPES intensity map at $E_F$. (b) Calculated FS. (c) Intensity plot and (d) momentum distribution curves of the ARPES data normal to the $\Gamma$-$M$ line (cut 1). ARPES data along cut 2 (e) and cut 3 (f) parallel to the $\Gamma$-$M$ line. The cut directions are shown in (a).

Now we focus on the needle-shaped FS on the $\Gamma$-$M$ line where a Dirac dispersion is expected. Figures 3(c), 3(e), and 3(f) are ARPES intensity plots along the cuts parallel or perpendicular to the $\Gamma$-$M$ line as indicated in Fig. 3(a). For cut 1, the raw data and the corresponding momentum distribution curves depicted in Fig. 3(d) show that the experimental band is almost linear at higher binding energies with $v_F^{\perp} \sim 2 \times 10^5$ m/s but appears to have some curvature near $E_F$. Such behavior is consistent with the calculated band for a shift of chemical potential $\sim 0.07$ eV in Fig. 3(c). In stark contrast, for cut 2 along the $\Gamma$-$M$ line, one can find an extremely dispersive band with a much larger $v_F$ [Fig. 3(e)]. While it is difficult to estimate the $v_F^{\parallel}$ in this cut due to strong overlap with the $\Gamma$-centered bands, we can estimate $v_F^{\parallel} \approx 1.1 \times 10^6$ m/s from the clear linear dispersion found along cut 3 [Fig. 3(f)], which is somewhat off from the $\Gamma$-$M$ line but still parallel to it as indicated in Fig. 3(a) [20]. This yields an anisotropy $v_F^{\parallel}/v_F^{\perp} \gtrsim 5$, in good agreement with the theoretical prediction.

As we have identified an anisotropic linear dispersion at a high energy scale, it will be important to investigate its chiral nature due to pseudospins. For that purpose, we have performed magnetotransport experiments in high magnetic fields. Figure 4(a) shows the in-plane magnetoresistivity ($\Delta\rho_{xx}$) and Hall resistivity ($\rho_{xy}$) as a function of the out-of-plane magnetic field. Clear Shubnikov-deHaas (SdH) oscillations in both $\rho_{xx}(H)$ and $\rho_{xy}(H)$ are observed. The oscillating component shows a periodic behavior in $1/B$ with a single frequency of $F = 152(5)$ T. By using the Onsager relation $F = (\Phi_0/2\pi^2)A_k$, where $\Phi_0$ is the flux quantum and $A_k$ is the cross-sectional area of the Fermi surface normal to the magnetic fields, $A_k$ is found to be 1.45(5) nm$^{-2}$, which corresponds to $\sim 0.7\%$ of the total area of the Brillouin zone. The $H$ or $T$ dependence of the oscillating amplitude [Fig. 4(b)] gives a cyclotron mass of $m_c = 0.29(2)\ m_e$ ($m_e$ denotes free electron mass) and a

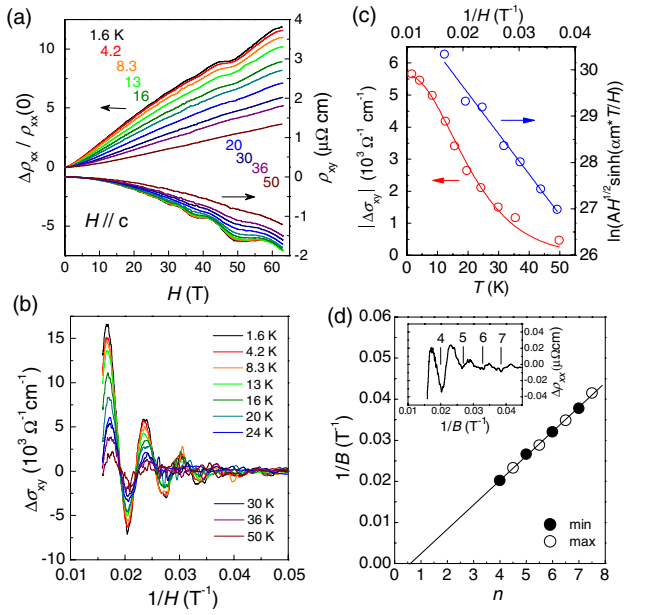


FIG. 4 (color online). (a) Magnetic field dependence of $\Delta\rho_{xx}(H)/\rho_0$ and $\rho_{xy}$ of $SrMnBi_2$. (b) Hall SdH oscillations $\Delta\sigma_{xy} = \sigma_{xy} - \langle\sigma_{xy}\rangle$ as a function of $1/H$ at various temperatures, where $\sigma_{xy} = \rho_{xy}/(\rho_{xx}^2 + \rho_{xy}^2)$. (c) Cyclotron mass and dingle plots for $\Delta\sigma_{xy}$. (d) SdH fan diagram plotting the measured $1/B_n$ with the filling factor $n$, which is estimated from the $\Delta\sigma_{xy}$ versus $1/B_n$ plot shown in the inset.

scattering time of $\tau = 3.5(5) \times 10^{-14}$ s$^{-1}$. The corresponding mobility $\mu = e\tau/m_c$ is ~250 cm$^2$/V s. A small FS, small effective mass, and relatively large mobility are consistent with the presence of Dirac fermions [21].

The key evidence for the existence of Dirac fermions is the nonzero Berry's phase associated with their cyclotron motion. According to a semiclassical magneto-oscillation description, the oscillation part of $\rho_{xx}$ follows $\Delta\rho_{xx} \sim \cos[2\pi(F/B + 1/2 + \beta)]$, where $\beta$ is the Berry's phase ($0 < \beta < 1$). Experimentally, the Berry's phase can be obtained from the analysis of the SdH fan diagram plotting $1/B_n$ as a function of the Landau index $n$ which can be determined from the minima of $\rho_{xx}$ as shown in the inset in Fig. 4(d). In the SdH fan diagram, the intercept of the linear fit yields the Berry's phase, which is expected to be $1/2$ for Dirac fermions in, e.g., monolayer graphene [22]. As shown in Fig. 4(d), the linear fit does not go through the origin but rather intercepts the abscissa at $n = 0.60(9)$. The resulting nonzero Berry's phase reveal that the low-density and high mobile carriers in $SrMnBi_2$ are indeed Dirac fermions.

Based on our findings, we conclude that the Bi square net in $SrMnBi_2$ hosts highly anisotropic Dirac fermions. This implies that $SrMnBi_2$-type compounds containing a Bi square net can be a new platform for anisotropic Dirac fermions with intriguing properties. For example, in $ATP_2$ ($A$ denotes an alkaline-earth-metal atom, $T$ a transition metal, and $P$ a pnictogen), the anisotropy of the Dirac cone can be tuned by introducing other alkaline-earth metals, and the SOC gap can also be tuned by replacing Bi with other pnictogens with lower atomic numbers. Furthermore, magnetism and superconductivity can also be incorporated into materials with Dirac fermions as found in a recently discovered superconductor $CeNi_xBi_2$ [23] and a hypothetical superconductor $BaFeP_2$ [24]. Therefore, our findings on Dirac fermions in a layered pnictide, $SrMnBi_2$, containing a square net provide new perspectives not only for controlling the anisotropy of the Dirac cone but also for coupling to magnetic or superconducting orders.

The authors thank Y. W. Son and H. W. Lee for fruitful discussion. This work was supported by LFRIR (2010-00471), BSR (2009-0076700), SRC (2011-0030046), and WCU (R32-2008-000-10180-0) programs through the NRF funded by the MEST. ARPES work was supported by the KICOS (No. K20602000008). Experimental work at the HLD was supported by EuroMagNET II (No. 228043). Y. J. J. is supported by the NRF (2010-0006377 and 2010-0020057).

*jhshim@postech.ac.kr
†js.kim@postech.ac.kr

[1] A. H. Castro Neto *et al.*, Rev. Mod. Phys. **81**, 109 (2009).
[2] M. Z. Hasan and C. L. Kane, Rev. Mod. Phys. **82**, 3045 (2010).
[3] C.-H. Park *et al.*, Nature Phys. **4**, 213 (2008).
[4] S.-M. Choi, S.-H. Jhi, and Y.-W. Son, Phys. Rev. B **81**, 081407(R) (2010).
[5] A. Kobayashi *et al.*, J. Phys. Soc. Jpn. **76**, 034711 (2007).
[6] G. Montambaux *et al.*, Phys. Rev. B **80**, 153412 (2009).
[7] V. Pardo and W. E. Pickett, Phys. Rev. Lett. **102**, 166803 (2009).
[8] P. Dietl, F. Piéchon, and G. Montambaux, Phys. Rev. Lett. **100**, 236405 (2008).
[9] W. Tremel and R. Hoffmann, J. Am. Chem. Soc. **109**, 124 (1987).
[10] Tetragonal structure ($I4/mmm$) with lattice constants $a = 4.565(2)$ Å and $c = 23.123(8)$ Å, consistent with the previous report [G. Cordier and H. Schaefer, Z. Naturforsch. B **32**, 383 (1977)].
[11] M. Weinert, E. Wimmer, and A. J. Freeman, Phys. Rev. B **26**, 4571 (1982).
[12] P. Blaha, K. Schwarz, G. K. H. Madsen, D. Kavasnicka, J. Luitz, WIEN2K (Karlheinz Schwarz, Technische Universitat Wien, Austria, 2001).
[13] J. P. Perdew, K. Burke, and M. Ernzerhof, Phys. Rev. Lett. **77**, 3865 (1996).
[14] The strong Néel order with high $T_N$ was also found in the structurally related $BaMn_2As_2$ ($T_N = 625$ K) and $BaMn_2P_2$($T_N > 750$ K). [Y. Singh *et al.*, Phys. Rev. B **80**, 100403(R) (2009); S. L. Brock *et al.*, J. Solid State Chem. **113**, 303 (1994).]
[15] C. Uher and W. P. Pratt, Phys. Rev. Lett. **39**, 491 (1977).

[16] The Néel ordering has lower energy than paramagnetic, ferromagnetic, and the stripe-type antiferromagnetic by 1.64, 0.55, and 0.09 eV/Mn, respectively.
[17] This is distinct from the 3D anisotropic Dirac FS found in bulk Bi, which originates from the dimer distortion in the rhombohedral structure.
[18] H. Min *et al.*, Phys. Rev. B **74**, 165310 (2006).
[19] C. L. Kane and E. J. Mele, Phys. Rev. Lett. **95**, 146802 (2005); S. Pandey *et al.*, arXiv:1107.0122.
[20] This value should be considered as a lower bound of $v_F^{\parallel}$ since the dispersion becomes less steep as the cut is shifted away from the Dirac point, here, from cut 2 to cut 3.
[21] The large FS centered at the $\Gamma$ point [Fig. 3(a)] has a negligible contribution to the SdH oscillations because its carriers have small mobility due to larger $m^*$ and shorter $\tau$ as seen in the ARPES data.
[22] Y. Zhang, Y.-W. Tan, H. L. Stromer, and P. Kim, Nature (London) **438**, 201 (2005).
[23] H. Mizoguchi *et al.*, Phys. Rev. Lett. **106**, 057002 (2011).
[24] J. H. Shim, K. Haule, and G. Kotliar, Phys. Rev. B **79**, 060501 (2009).